LANGMUIR Article
Cite This: Langmuir 2019, 35, 5342−5352
pubs.acs.org/Langmuir

Velocity Saturation in Digital Microfluidics

Ian Swyer,[†,∥] Ryan Fobel,[‡,∥] and Aaron R. Wheeler*[,†,‡,§]

[†]Department of Chemistry, University of Toronto, 80 St. George Street, Toronto, ON M5S 3H6, Canada
[‡]Donnelly Centre for Cellular and Biomolecular Research, University of Toronto, 160 College Street, Toronto, ON M5S 3E1, Canada
[§]Institute for Biomaterials and Biomedical Engineering, University of Toronto, 164 College Street, Toronto, ON M5S 3G9, Canada

Supporting Information

ABSTRACT: In digital microfluidics, discrete droplets of fluid are made to move on an open surface with no microchannels. These systems are commonly operated by application of electrical driving forces to an array of electrodes. While these driving forces are well characterized, the dissipative forces opposing droplet movement have not been as thoroughly examined. In recognition of this deficit, we used force−velocity plots to characterize droplet movement in digital microfluidics, which was found to be consistent with a simple theoretical framework for understanding dissipation effects for droplets in two-plate, air-filled devices. Interestingly, in some conditions, a previously unreported "velocity saturation" effect was observed. When examined across a range of different liquids, the forces at which this saturation occurs seem to be lower for liquids with smaller surface tensions. Furthermore, when driven at forces that cause saturation, physical phenomena are observed that are akin to what has been reported for stationary droplets in the electrowetting literature. These phenomena are detrimental to device performance, leading to a new "force window" approach that delineates the optimum operation conditions for different liquids. We propose that these findings may be useful for a wide range of applications for experts and new users alike in this growing field.

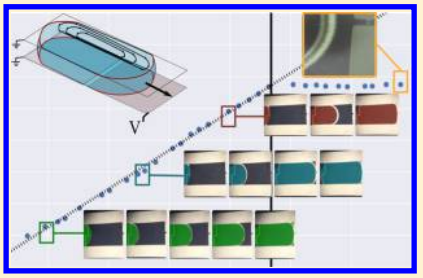

INTRODUCTION

Digital microfluidics (DMF) uses electrical,[1−3] thermocapillary,[4,5] magnetic,[6,7] acoustic,[8] or mechanical[9] forces to manipulate discrete droplets on an open surface with no channels. Electrical actuation, which is used here, is the most common paradigm, in which droplets are moved, mixed, and split in response to electric fields that are applied to an array of insulated electrodes. In this paper, we differentiate between DMF systems, in which droplets are made to move across an array of electrodes (either in "one-plate" mode with driving and counter electrodes on the same substrate, or in "two-plate" mode with driving and counter electrodes on different substrates), from sessile droplet/electrowetting experiments, in which stationary droplets are made to change their shape on a single electrode. The two phenomena are related but also have some distinct features.

DMF has become popular in recent years for a wide range of applications, including automated cell culture and analysis,[10−12] multiplexed chemical synthesis,[13,14] and parallel-scale clinical sample testing.[15−17] The physics of the diving force in DMF is similar to that of dielectrophoresis in that an applied electric field polarizes the liquid droplet and this polarization is then acted on by the applied field.[18,19] Serendipitously, this complex process lends itself to a simple electromechanical circuit model equivalence to determine the driving force on a droplet.[20] These simple circuit models have proven to provide reliable correlation with experimental results for a wide range of fluids.[21,22]

While the driving forces behind droplet movement in DMF are well understood, the dissipative mechanisms in DMF are markedly less characterized, making it surprisingly difficult to predict or explain seemingly basic operating characteristics, for example, the relative ease with which different liquids can be manipulated or the effect of different operating conditions on droplet movement and device longevity. In an early examination of this topic, Ren et al.[23] showed empirically that dissipative forces in droplets moving in a DMF device are dominated by (1) contact line friction, followed by (2) viscous drag of the suspending medium, and then (3) internal viscous dissipation. Contact line friction is a resistive force that arises from altering the adsorption/desorption kinetics of solvent and solute molecules in the advancing contact line between the liquid droplet and solid surface.[24] This force was also demonstrated to be the most important dissipative mechanism for the related systems of electromechanical actuation of a column of liquid in a parallel plate capacitor and for droplets being made to move by gravity between planar, vertical substrates.[25,26] Viscous drag arises from the surrounding medium (e.g., an immiscible oil, as in Ren et al.[23]) impeding the droplet as it moves; when this medium is air (as is the case for the experiments and model described here), this contribution is negligible. Internal viscous dissipation is a

Received: January 24, 2019
Revised: March 12, 2019
Published: April 8, 2019

DOI: 10.1021/acs.langmuir.9b00220
Langmuir 2019, 35, 5342−5352

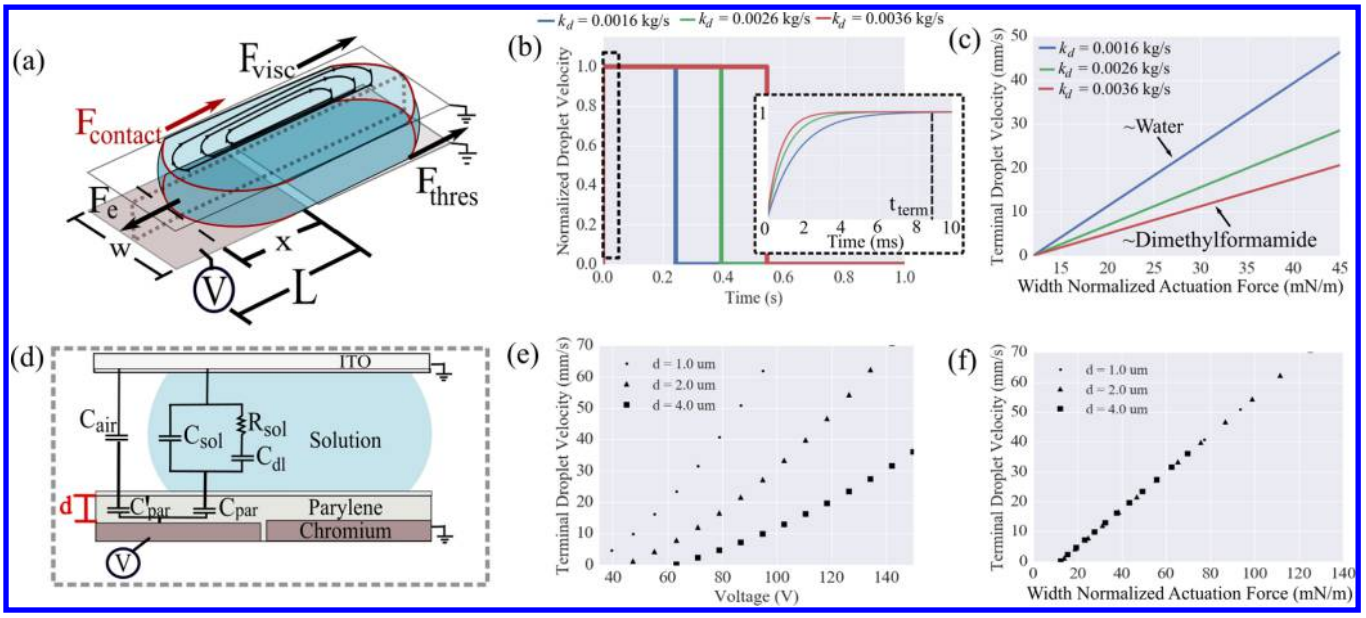

Figure 1. Model of droplet dynamics in DMF. (a) Schematic showing the relevant forces on a droplet as it moves onto a destination electrode under applied potential V, including the electrostatic driving force F_e, as well as dissipative forces—the viscous recirculation force F_{visc}, the contact line friction force $F_{contact}$ (in red), and the threshold force F_{thres}. (b) Predicted normalized droplet velocities as a function of time for droplets with different total velocity-sensitive dissipation coefficients k_d = 0.0016 (blue), 0.0026 (green), and 0.0036 (red) kg/s, driven at width-normalized force f_e = 25 mN/m. The inset is a magnified view of initial times (represented by the dashed box in the main panel), illustrating the time t_{term} required to achieve terminal velocity v_{term}. As shown, all droplets achieve v_{term} within 10 ms, indicated by the dashed black line. (c) Predicted droplet velocities as a function of width-normalized driving force for droplets with k_d = 0.0016 (blue), 0.0026 (green), and 0.0036 (red) kg/s. (d) Equivalent circuit for the digital microfluidic device shown in panel (a), with ITO electrode on the top plate and chromium electrodes on the bottom plate coated with the dielectric Parylene C with thickness d (in red). Circuit components include capacitances of air, the Parylene C layer underneath the air, the Parylene C layer underneath the droplet, the double layer formed at the interface of the droplet and the bottom-plate device surface, and the bulk solution in the droplet, as well as the bulk resistances in the droplet: C_{air}, C'_{par}, C_{par}, C_{dl}, and C_{sol}, and R_{sol}, respectively. (e) Predicted droplet velocities as a function of driving voltage for an aqueous droplet with high conductivity on devices with Parylene C dielectric thicknesses d = 1.0 (circles), 2.0 (triangles), and 4.0 μm (squares). (f) Predicted droplet velocities for the same conditions (and symbols) as in panel (e) as a function of width-normalized driving force.

consequence of momentum transfer between different laminas in the droplet. The exact relationship between this dissipation and the applied force on the droplet can be complex, as the internal circulation in droplets manipulated on DMF devices[27] is similar to that observed in droplets traveling through a microfluidic channel[28] as seen by particle imaging velocimetry studies. Why this is true has not been explored, and therefore, there is no analytic model to estimate this force. The final force to consider that opposes droplet movement is the threshold force (i.e., the force required to initiate droplet movement), which is associated with contact line pinning and contact angle hysteresis.

In addition to the dissipative forces that oppose droplet movement in DMF described above, the sessile droplet/electrowetting literature describes additional mechanisms that may become important when high voltages are applied. For example, it is widely known that the contact angles in such systems decrease parabolically with respect to applied voltage following the well-known Young−Lippmann equation at low voltages but that, at high voltages, a "contact angle saturation" phenomenon is observed in which solid−liquid contact angles deviate from the equation to change more slowly or stop changing altogether. Given the similarity between electrowetting systems and DMF, one might expect similar observations for droplet velocity in DMF devices. Surprisingly, though, while many authors[23,29,30] have reported a parabolic trend in droplet velocity with respect to applied voltage, there has been little discussion of velocity saturation effects in DMF. Specifically, we are aware of only one previous study, from Bavière et al.,[31] that reported a velocity saturation effect. In this study,[31] a high-frame-rate camera captured images of an aqueous droplet moving on a one-plate DMF device—at low voltages, the velocity trend was parabolic with respect to voltage, but at high voltages, droplet velocity was observed to saturate or to increase more slowly than predicted. In a companion experiment evaluating sessile droplets actuated by electrowetting, the authors observed that the contact angle and velocity saturations occurred at roughly the same applied voltage. We propose that the Bavière et al.[31] study is a fundamentally important one for the field, but note that it evaluated only the one-plate mode rather than the much more common two-plate DMF configuration (i.e., the configuration that has inspired so many interesting and diverse applications[10−17]).

Here, we seek to extend the study of velocity saturation to two-plate DMF device actuation and to provide a framework that is currently missing for the connection between droplet velocity and the dissipation mechanisms that oppose droplet movement. We introduce a simple, on-chip characterization method that relies on capacitance-based measurements of droplet velocity collected over a range of applied electrostatic forces to generate a force−velocity plot, from which we can extract several useful parameters including threshold and velocity-saturation forces. Importantly, this method is fast (requiring only a few seconds of droplet movement) and fully automated, meaning that it can be easily integrated into

DOI: 10.1021/acs.langmuir.9b00220
Langmuir 2019, 35, 5342−5352

routine DMF experiments, enabling real-time, quantitative, force-based diagnostics and rapid characterization of new liquids on-chip prior to use. Importantly, we present a substantial body of evidence to support the observation of velocity saturation in two-plate DMF devices and furthermore connect this phenomenon to the onset of phenomena described in the electrowetting literature for high applied voltages, that is, satellite-droplet ejection[32,33] or the related phenomena of corona discharge, charge injection, and localized dielectric breakdown.[33−39] We also show that droplet contents determine the types of saturation phenomena that are observed and in particular that additives that are commonly used to reduce biofouling (and that coincidentally, reduce surface tension) can decrease the saturation force, which imposes limits to the range of useful operating conditions. The capability to measure the velocity-saturation force is a fundamentally important contribution to the DMF toolbox because it determines the maximum force that can be applied to a liquid droplet without causing undesirable effects. For example, we report (for the first time) experimental evidence that operating devices at conditions above the saturation force can lead to irreversible device damage, a result that has important implications for device reliability and longevity.

THEORY

The translation of a droplet in a DMF device is an inherently complex process involving internal three-dimensional flows,[27,40] droplet deformation,[41] and contact line dynamics that are not fully understood.[42,43] To simplify the system of analysis here, we make the assumption that each droplet moves as a solid body without changing its shape in the x−y plane, that is, a quasistatic assumption. This simplified analysis does not account for known droplet-shape subtleties (e.g., droplets have been reported to elongate by ∼5% during actuation in DMF devices[41]); however, it provides a reasonable estimate of droplet position as a function of time, which is sufficient for the questions that were asked here. In general, the quasistatic assumption is appropriate when inertial forces are small relative to surface tension and viscous forces. This is the case for all experiments described here, as described in Section S1 in the Supporting Information.

Consider the case of a flat bus-shaped droplet (rectangular in the middle, capped with semicircles on the ends) on a DMF device with rectangular electrodes with lengths L and widths w. The droplet moves from an initial electrode to a destination electrode that is excited with an ac potential V, as shown in Figure 1a. In this analysis, we assume that the time constant of the electrical circuit is much shorter than that of droplet acceleration/deceleration, as described in Section S2 in the Supporting Information. Finally, we limit our discussion to times t in which the leading edge of the droplet has already completely overlapped with the leading edge of the destination electrode, such that the droplet has traveled a distance x onto the destination electrode; at this point, the flow can be considered to be fully developed.

Consider the electrostatic force F_e that drives the droplet onto the destination electrode and dissipative forces that oppose movement, including the internal viscous force F_{visc}, the contact line friction force $F_{contact}$, and the threshold force F_{thres}. Theory predicts that F_{visc} and $F_{contact}$ are linearly proportional to droplet velocity v,[23,24] so we define velocity-sensitive dissipation coefficients k_{visc} and $k_{contact}$, respectively. With the caveats and assumptions indicated above, a force balance yields the following equations (with droplet mass and acceleration m and a, respectively):

$$ma = F_e(t) - F_{thres} - F_{visc} - F_{contact}$$

$$\frac{dv}{dt} + \frac{k_{visc} + k_{contact}}{m}v = \frac{F_e(t) - F_{thres}}{m}$$

This ordinary differential equation can be readily solved to give eq 1, where the total velocity-sensitive dissipation coefficient is $k_d = k_{visc} + k_{contact}$.

$$v = \frac{F_e - F_{thres}}{k_d}(1 - e^{-k_d/mt}) - \frac{F_e}{k_d}(1 - e^{-k_d/m(t-b)})u(t - b) \quad (1)$$

The treatment above assumes that the actuation voltage is "on" at $t = 0$ and remains on until $t = b$, at which time it is turned "off"; this leads to the step function $u(t - b)$ in the second term of eq 1. In reality the actuation force does not decrease as a unit step, as the leading edge of the droplet does not reach the trailing edge of the destination electrode at the same time. Future studies may look more in detail at the acceleration/deceleration stages of droplet movement, but this approximation is reasonable here, as our goal is to understand how a droplet begins moving and continues to move, rather than how it stops, and the discussion below focuses solely on the first term in eq 1. Finally, it is useful to normalize the forces acting on the droplet as a function of electrode width (e.g., f_e and f_{thres})

$$f_e = \frac{F_e}{w} \quad \text{and} \quad f_{thres} = \frac{F_{thres}}{w}$$

giving eq 2.

$$v = \frac{w(f_e - f_{thres})}{k_d}(1 - e^{-k_d/mt}) \quad (2)$$

Figure 1b shows the width-normalized velocities predicted by eq 1 for three droplets with varying k_d as they move onto the destination electrode, all driven at constant force. As shown, the velocities increase rapidly from zero to their terminal (or maximum) value v_{term} and then return to zero when the leading edge of the droplet reaches the trailing edge of the destination electrode. As expected, droplets with lower k_d complete the movement more rapidly; interestingly, as shown in the inset, droplets with lower k_d also require more time t_{term} to reach v_{term}. In experiments with a range of different liquids (described below), the largest t_{term} was found to be ∼9 ms (for pure water). Thus, in the model, v_{term} was defined (for all liquids) as being the velocity predicted at t = 10 ms. Figure 1c shows the predicted terminal velocities for three droplets with varying k_d as a function of width-normalized driving force f_e. As indicated, the trends are linear, with fluids with lower k_d having larger v_{term}. Note that the high velocity (k_d = 0.0016 kg/s) and low velocity (k_d = 0.0036 kg/s) cases approximate experimental observations for droplets of water and dimethylformamide, respectively.

The devices used here include top plates with an indium tin oxide (ITO) electrode and bottom plates with chromium driving electrodes coated with Parylene C dielectric with thickness d. [Note that in experiments, a thin (50 nm) Teflon AF layer is spin-coated on top of the Parylene C layer, but it is ignored in this discussion as it makes negligible contributions to the equivalent circuit.] An electromechanical circuit model

DOI: 10.1021/acs.langmuir.9b00220
Langmuir 2019, 35, 5342−5352

used to predict the actuation force for an aqueous droplet suspended in air is shown in Figure 1d, where C_{air}, C'_{par}, C_{par}, C_{dl}, and C_{sol} are the capacitances of air, the Parylene C layer underneath the air, the Parylene C layer underneath the droplet, the double layer formed at the bottom of the droplet, and the bulk solution in the droplet, respectively. The only component with resistance that must be considered is the droplet, modeled as R_{sol}.

In the case of most commonly used liquids in DMF, the total impedance of the droplet is insignificant relative to the impedance of the dielectric layer for actuation frequencies at or below 10 kHz. This condition is commonly referred to as being within the "electrowetting" regime,[44,45] in which the droplet (i.e., C_{dl}, C_{sol}, and R_{sol}) acts as a short circuit. As a further approximation, we can ignore the capacitances of the air and the dielectric beneath the the air (i.e., C_{air}, C'_{par}), as they do not contribute significantly to the total capacitive energy stored in the system. Finally, we note that the approximations described above are true for nearly all relevant values of x. To summarize, the force on the droplet is given by the following expressions,

$$F_e = \frac{1}{2}\frac{d(C_{par}V_{RMS}^{\ 2})}{dx}$$

$$f_e = \frac{F_e}{w} = \frac{\epsilon_o \epsilon_{par} V_{RMS}^{\ 2}}{2d} \quad (3)$$

where ϵ_o is the permittivity of free space and ϵ_{par} is the relative permittivity of Parylene C. Given the approximations above, we can use eq 3 to generate the width-normalized driving force term for eq 2, and upon doing so, the expected parabolic relationship between applied voltage and droplet velocity is revealed, as shown in Figure 1e. This type of voltage−velocity plot is highly sensitive to the the thickness of the dielectric layer of the DMF device. In experiments, if the dielectric layer thickness varies between devices (or even between different regions in the same device), this can cause significant errors in data interpretation. Thus, in this work, we eliminate the sensitivity to the dielectric thickness by considering velocity as a function of width-normalized driving force (instead of voltage). As shown in Figure 1f, this approach reveals a unified, linear relationship between force and velocity for all conditions.

The prediction of an unvarying linear relationship between driving force and velocity (Figure 1f) is central to the experiments and their interpretations reported here. Specifically, we define any deviations from the initial and predicted linear trend to be saturation phenomena and seek to connect them (if observed) to what is known about sessile droplets/electrowetting and/or to DMF device performance.

RESULTS AND DISCUSSION

Force−Velocity Plots and Saturation. The goal of this work was to develop a framework that could provide insight into the various dissipation mechanisms that oppose droplet mobility in two-plate digital microfluidics. As a first step toward this goal, we evaluated the fidelity of the simple model given in the Theory section (outlined in Figure 1) to experimental observations. Figure 2 shows experimental observations for three droplets of an aqueous solution of 0.1 mg/mL L64 with 0.1 M NaCl being driven onto a destination electrode at different driving forces. This liquid is a representative of the aqueous buffers commonly used in many biological applications and hence is of great practical importance. As shown, capacitance measurements are converted to positions along the axis of movement and are plotted relative to time in Figure 2a. Note that the capacitive measurement employed here is straightforward—at each time, a position corresponding to the droplet's center-of-mass is estimated on the basis of the extent of its overlap with the destination electrode. Corresponding droplet positions (determined optically) for these capacitive measurements can been seen in Figure 2b, illustrating good fidelity between the two techniques. This relationship is examined in more detail in Figure S1 and in Section S3 of the Supporting Information. An advantage of the capacitance-derived position measurements (in contrast to those generated from images) is that they can be made rapidly and converted to instantaneous velocities, shown by the discrete markers in Figure 2c. These measurements (while noisy) are constant over the time course of droplet movement, representing the achievement of terminal velocity for each of these force steps. The solid lines in Figure 2c are generated from eq 2 with f_{thres} = 10 mN/m, k_d = 0.0038

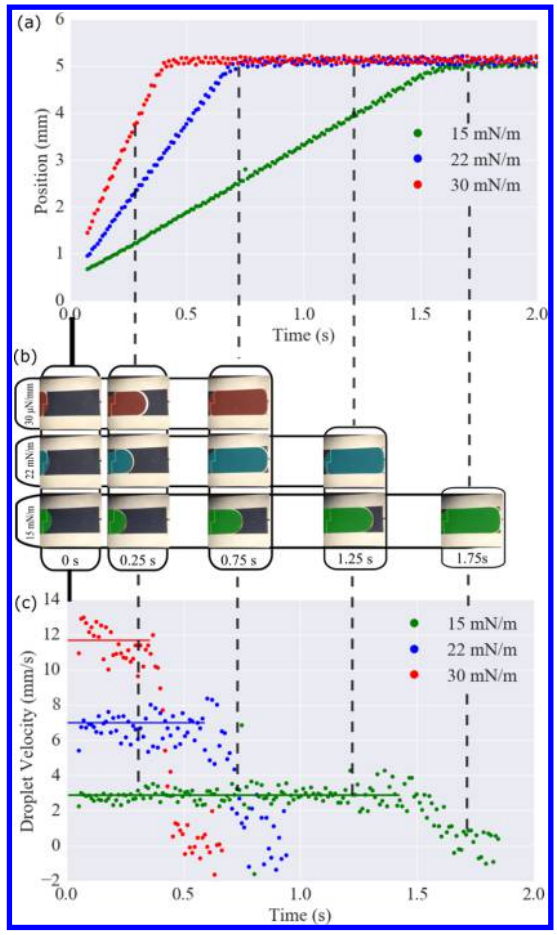

Figure 2. Experimental characterization of droplet dynamics in DMF. (a) Representative plots of x-axis position (measured by capacitance) as a function of time for 2.8 μL aqueous droplets (each containing 0.1 mg/mL L64 + 0.1 M NaCl) driven onto a charged 2.25 × 5.2 mm electrode with width-normalized driving forces of 15 (green), 22 (blue), or 30 (red) mN/m. (b) Representative images of droplets corresponding to the conditions in panel (a) at t = 0, 0.25, 0.75, 1.25, and 1.75 s. Each image was pseudocolored to highlight the droplet position. (c) Representative plots of instantaneous velocity (discrete markers) as a function of time for the conditions in panel (a). Solid lines indicate the terminal velocities predicted by eq 2.

DOI: 10.1021/acs.langmuir.9b00220
Langmuir 2019, 35, 5342−5352

kg/s, w = 2.25 mm, $m = 2.8 \times 10^{-6}$ kg, and t > 10 ms; it is apparent that the measurements are in line with the theoretical predictions. Finally, we note that the maximum velocity that can be reliably measured using the system described here is approximately 20 mm/s; velocities above this limit can be determined, but they suffer from poor precision, as the small number of measurements makes the assignment of terminal velocity highly sensitive to outliers. Future versions of the measurement system might alleviate this limit by enabling higher frequency capacitance measurements, but the current system was adequate for the results presented here.

The central tool used in this work is the so-called force–velocity plot in which droplet velocities are measured as a function of driving force as shown in Figure 3. There are two

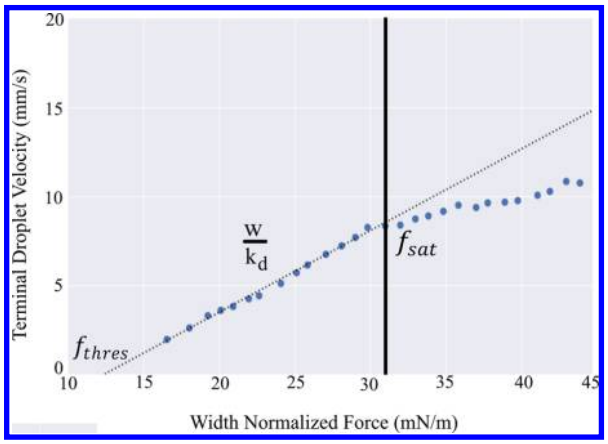

Figure 3. Force–velocity plot. Terminal droplet velocity (blue markers) measured as a function of width-normalized driving force for an aqueous droplet containing 0.1 mg/mL L64 and 0.1 M NaCl. The width-normalized threshold force f_{thres} = 12.4 mN/m (x-axis intercept) and saturation force f_{sat} = 31 mN/m (black vertical line) are indicated, as well as a dashed line with a slope proportional to the inverse of the total velocity-sensitive dissipation coefficient k_d = 0.0049 kg/s.

key features of a force–velocity plot that are important for understanding the results presented here. The first feature to note is that at low driving forces, the relationship is linear, as is predicted by eq 2. For the data shown in Figure 3, in this low-force region, the total velocity-sensitive dissipation coefficient (arising from internal viscous dissipation and contact line friction) is k_d = 0.0049 kg/s, and the threshold force (the minimum applied force necessary to initiate droplet movement) is f_{thres} = 12.4 mN/m. The second feature to highlight is the observation that as driving force is increased above a particular level (i.e., in Figure 3, this level is f_e = 31 mN/m), the initial linear trend predicted by eq 2 is violated. We call this level the saturation force f_{sat}, as an analogy to the well-known contact angle saturation effect described in the sessile droplet/electrowetting literature. Bavière et al.[31] reported a phenomenon similar to f_{sat} for one-plate digital microfluidics, but as far as we are aware, this is the first report of velocity saturation in two-plate digital microfluidics. In an attempt to better understand this phenomenon, we studied saturation behavior in two classes of liquids that are commonly used in digital microfluidics—those with low and high conductivities, described below.

Velocity Saturation in Liquids with Low Conductivity. Most digital microfluidic experiments involve the manipulation of aqueous droplets; when no external inorganic salts are added, these liquids have relatively low conductivity. Further, aqueous solutions in digital microfluidics are often modified to contain nonionic surfactants to limit the effects of biofouling.[46−48] With this in mind, we began our work by evaluating aqueous droplets containing the commonly used surfactant additive Pluronic L64. A force–velocity plot for 0.1 mg/mL L64 is shown in Figure 4a. As indicated, the average saturation

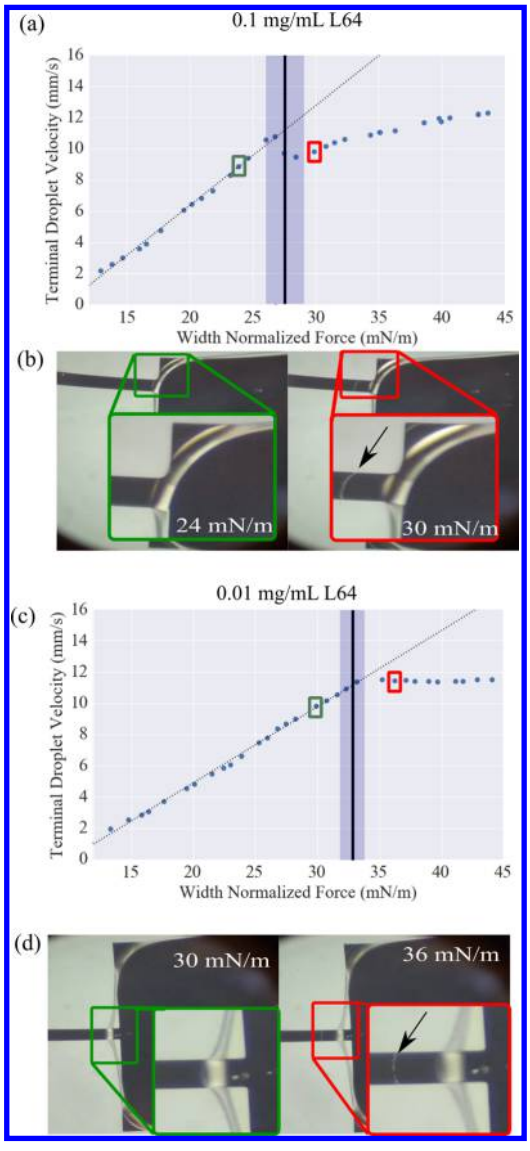

Figure 4. Velocity saturation and satellite-droplet ejection in aqueous surfactant. (a,c) Representative force–velocity plots (blue markers) for aqueous droplets containing 0.1 [average f_{sat} = 27.5 ± 1.5 mN/m (n = 8)] and 0.01 mg/mL L64 [average f_{sat} = 32.8 ± 1 mN/m (n = 10)]. The initial linear trends are shown as dashed black lines, the average saturation forces are identified with solid black vertical lines, and forces within 1 SD of the average saturation force are denoted by light blue boxes. Red and green boxes in panels (a) and (c) correspond to the images in panels (b) and (d) of droplets after manipulation at forces below (left) and above (right) the respective saturation forces for the two solutions (i.e., f_e = 24 and 30 mN/m for 0.1 mg/mL L64, and f_e = 30 and 36 mN/m for 0.1 mg/mL L64). Insets outlined in green (left, $f_e < f_{sat}$) and red (right, $f_e > f_{sat}$) are magnified images of the edges of the droplets in which black arrows indicate the observation of ejected satellite droplets for $f_e > f_{sat}$.

DOI: 10.1021/acs.langmuir.9b00220
Langmuir 2019, 35, 5342−5352

force is f_{sat} = 27.5 ± 1.5 mN/m (n = 8; raw data in Figure S2). Magnified images of droplets on a device after actuating at $f_e < f_{sat}$ and $f_e > f_{sat}$ are shown in green and red outlines in Figure 4b, respectively. Interestingly, the image of the droplet that moved at $f_e > f_{sat}$ shows the existence of ejected satellite droplets (this effect is most obvious in Video M1). This phenomenon has been reported in the sessile droplet/electrowetting literature,[32,33] but as far as we are aware, this is the first report of the phenomenon for moving droplets in DMF. We hypothesize that droplet ejection (at least partly) serves as an additional dissipation mechanism for droplets manipulated above the saturation force, causing the deviation from the linear trend at low forces predicted by eq 2.

The observation of satellite-droplet ejection for $f_e > f_{sat}$ (and not for $f_e < f_{sat}$) was consistent for many repeated experiments with a range of fluids with low conductivity. For example, the force–velocity plot for a solution with a different concentration of surfactant (0.01 mg/mL L64) is shown in Figure 4c. Note that the average saturation force for this solution, f_{sat} = 32.8 ± 1 mN/m (n = 10; raw data in Figure S3), is higher than that for the more concentrated solution. Images of droplets that moved at $f_e < f_{sat}$ and $f_e > f_{sat}$ (with satellite droplet formation) are shown in Figure 4d. Note that satellite-droplet ejection in DMF is not desirable, as it can result in cross-contamination between different samples manipulated on the device; furthermore, satellite droplets evaporate rapidly, which can leave behind dried spots of solute that can cause droplet pinning.

While aqueous solutions are used for many applications of digital microfluidics, applications involving chemical synthesis[13,14] typically require the use of organic solvents. With this in mind, we decided to evaluate the behavior of dimethylformamide, a polar organic solvent used in a wide range of syntheses and related applications. A representative force–velocity plot for dimethylformamide is shown in Figure 5a. As is apparent, the trend is more complex for dimethylformamide than for the aqueous solutions in Figures 3 and 4. That is, droplet velocity for dimethylformamide is linear at low forces, but velocities actually begin to decrease with increasing force (highlighted in green and blue boxes), until plateauing at higher force (highlighted in the red box). In replicate analysis, the average saturation force for this fluid was f_{sat} = 20.3 ± 1.6 mN/m (n = 14; raw data in Figure S4). As shown in Figure 5b, satellite-droplet ejection is observed for $f_e > f_{sat}$ for dimethylformamide, and the number and size of the ejected satellite droplets seem to increase with higher forces (this observation is readily apparent in Video M2). More study is needed, but we hypothesize that the complex velocity trends for dimethylformamide at $f_e > f_{sat}$ (relative to aqueous surfactant solutions) is a function of the increased severity of satellite-droplet ejection for this fluid.

Velocity Saturation in Liquids with High Conductivity. Digital microfluidics is often used for applications[10−12,15−17] that require aqueous solutions containing high concentrations of inorganic salts (which renders the droplets highly conductive). Aqueous sodium chloride was used as a model system here to evaluate the potential existence of saturation effects in such liquids. As a first step, a simple 0.1 M NaCl solution with no other additives was evaluated, with a representative force–velocity curve in Figure 6a. We speculate that there may be a saturation force for 0.1 M NaCl (perhaps at f_e > 45 mN/m), but it was not observable within the velocity limits measurable with our current apparatus (described above). Velocity saturation for high velocity/high surface tension droplets remains an interesting question for future studies, but the vast majority of DMF applications utilize surfactants (to prevent biofouling and/or facilitate droplet splitting) or other solvents that have lower surface tension, for which the maximum droplet velocities are well within the measurable range of our system.

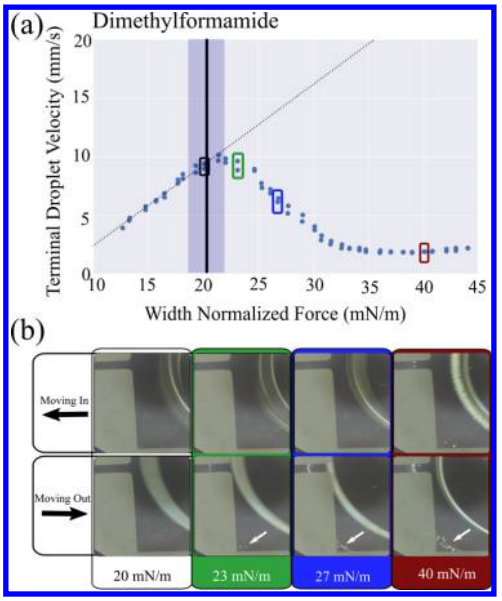

Figure 5. Velocity saturation and satellite-droplet ejection in dimethylformamide. (a) Representative force–velocity plot (blue markers) for a dimethylformamide droplet. The initial linear trend is shown as a dashed black line, the average saturation force (20.3 mN/m) is identified with a solid vertical black line, and the forces within 1 SD of the average saturation force (±1.6 mN/m, n = 14) are denoted by the light blue box. Boxes highlight droplet velocities observed below saturation at f_e = 20 mN/m (black) and above saturation at f_e = 23 (green), 27 (blue), and 40 mN/m (red). (b) Images of dimethylformamide droplet moving onto (top) and away from (bottom) the destination electrode. Image-outline colors correspond to the driving forces highlighted in panel (a): 20 (black), 23 (green), 27 (blue), and 40 mN/m (red). White arrows indicate the observation of ejected satellite droplets for $f_e > f_{sat}$.

Examples of force–velocity plots for aqueous solutions of 0.1 M NaCl containing 0.01 and 0.1 mg/mL L64 are shown in Figure 6b,c, respectively. As indicated, both solutions exhibit obvious velocity saturation. The average saturation forces for 0.1 M NaCl containing 0.01 and 0.1 mg/mL L64 are 35.8 ± 1.5 mN/m (n = 10; raw data in Figure S5) and 31.1 ± 1.6 mN/m (n = 12; raw data in Figure S6), respectively. However, as indicated in the inset images (and in Video M3), unlike the solutions with low conductivity described above, no satellite-droplet ejection was observed (at driving forces above or below f_{sat}). This observation is not necessarily surprising, as the repression of satellite-droplet ejection in solutions with high conductivity has been reported in the sessile droplet/electrowetting literature.[33]

The velocity saturation that is apparent in the force–velocity plots in Figure 6b,c in the absence of satellite-droplet ejection suggests that there must be some other mechanism that contributes to force dissipation for droplets driven at $f_e > f_{sat}$. The sessile droplet/electrowetting literature describes a number of related phenomena that may play a role in such cases, including corona discharge, charge injection, and/or

DOI: 10.1021/acs.langmuir.9b00220
Langmuir 2019, 35, 5342−5352

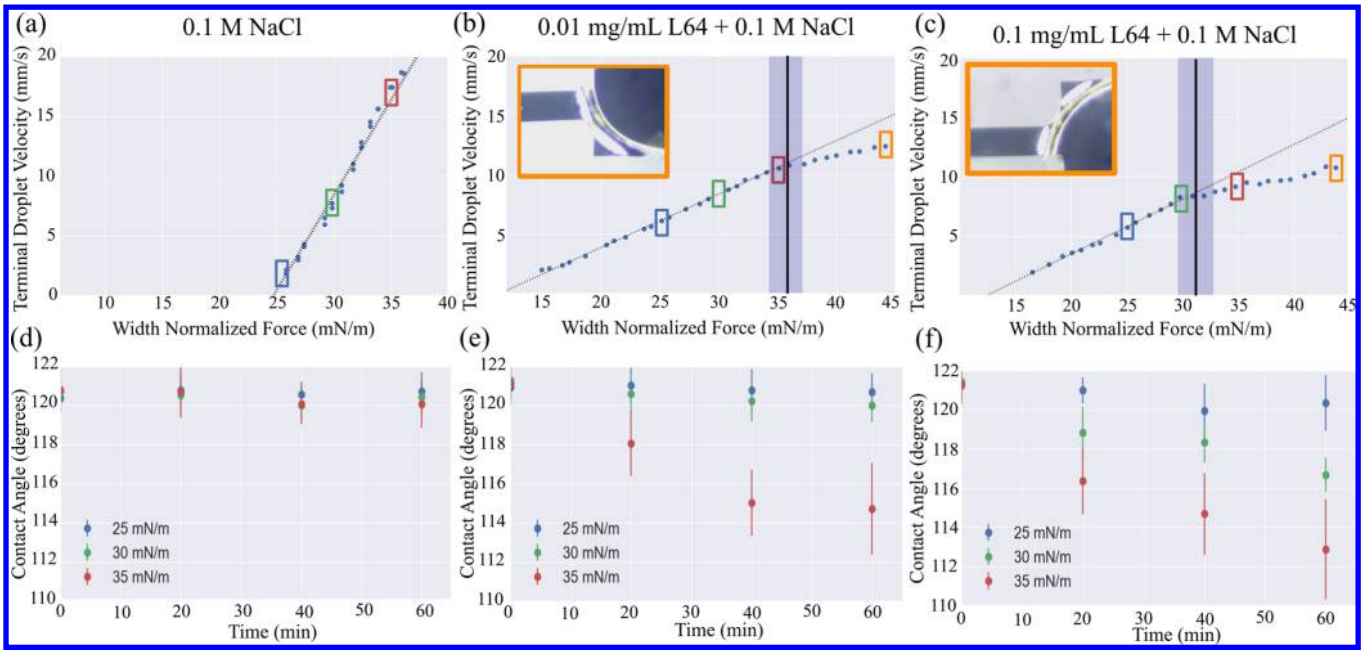

Figure 6. Velocity saturation and device degradation in droplets with high conductivity. Representative force−velocity plots (blue markers) for aqueous solutions of (a) 0.1 M NaCl, (b) 0.1 M NaCl + 0.01 mg/mL L64 [average f_{sat} = 35.8 ± 1.5 mN/m (n = 10)], and (c) 0.1 M NaCl + 0.1 mg/mL L64 [average f_{sat} = 31.1 ± 1.6 mN/m, (n = 12)]. [Note that the plot in panel (c) is identical to that in Figure 3; all replicates for this condition can be found in Figure S6.] The initial linear trends are shown as dashed lines, the average saturation forces are identified with solid black vertical lines, and the forces within 1 SD of the average saturation force are denoted by light blue boxes. Blue (25 mN/m), green (30 mN/m), and red (35 mN/m) boxes highlight the forces used to test contact angle changes over time. Orange boxes in panels (b) and (c) highlight droplet velocities observed at f_e = 44 mN/m (above f_{sat} for both conditions), corresponding to images in the insets of droplets immediately after being driven at these forces. Aqueous contact angles measured on DMF device surfaces after 20, 40, or 60 min of continuous droplet actuation for aqueous solutions of (d) 0.1 M NaCl, (e) 0.1 M NaCl + 0.01 mg/mL L64, and (f) 0.1 M NaCl + 0.1 mg/mL L64. Data correspond to droplets driven at f_e = 25 (blue), 30 (green), or 35 mN/m (red). Error bars indicate ±1 SD for n = 18 measurements per condition.

localized dielectric breakdown.[33−36] These phenomena are often described as being associated with device damage, and with this in mind, we decided to test for changes in hydrophobicity (as a proxy for device damage) by monitoring aqueous contact angles on DMF devices after continuous droplet manipulation at different forces for different durations. The same solutions from Figure 6a−c were manipulated at f_e = 25, 30, and 35 mN/m, and the corresponding contact angle measurements are shown in Figure 6d−f. As indicated, all of the contact angles began at values similar to what is expected for Teflon AF (∼120°). Furthermore, for each case in which f_e was substantially lower than f_{sat} (that is, 0.1 M NaCl at all driving forces, 0.1 M NaCl with 0.01 mg/mL L64 at f_e = 25 and 30 mN/m, and 0.1 M NaCl with 0.1 mg/mL L64 at f_e = 25 mN/m), the contact angle remained approximately unchanged throughout the experiment. However for each case in which f_e was close to or greater than f_{sat} (that is, 0.1 M NaCl with 0.01 mg/mL L64 at f_e = 35 mN/m and 0.1 M NaCl with 0.1 mg/mL L64 at f_e = 30 and 35 mN/m), the contact angle decreased significantly as time progressed. Further, in nearly all cases in which f_e was at least 5 mN/m greater than f_{sat}, it was observed that either (i) droplet velocity decreased after repeated actuation or (ii) droplets deformed into irregular shapes after repeated actuation—both observations are consistent with device damage. Overall, these observations support the hypothesis that corona discharge, charge injection, and/or localized dielectric breakdown[33−36] may contribute to energy dissipation for droplets with high conductivity manipulated at $f_e > f_{sat}$. As far as we are aware, these phenomena have not been reported before for two-plate digital microfluidics. This is surprising, as the data suggest that DMF users who work with droplets with high conductivity and operate devices with f_e greater than f_{sat} risk device degradation, which may eventually lead to device failure.

Velocity Saturation and the Force-Window Approach. As described herein, we report the first observation of velocity saturation in two-plate digital microfluidics. Furthermore, when forces greater than the saturation force are applied to droplets in such devices, satellite-droplet ejection is observed for liquids with low conductivity, and modification of device hydrophobicity is observed for liquids with high conductivity; these observations mirror those of the sessile droplet/electrowetting literature. These high-force phenomena are problematic for many applications, suggesting that users should carefully avoid working in conditions with f_e above f_{sat}. However, in addition to acknowledging the existence of velocity saturation, it is also instructive to evaluate how velocity saturation (and other observable dissipation phenomena) varies as a function of droplet composition.

We propose a new metric for evaluating DMF operation—the force window—that is bound at the "bottom" by the threshold force and at the "top" by saturation force. Force windows for each of the solutions evaluated here are shown in Figure 7, plotted as a function of liquid surface tension to illustrate some interesting trends. As shown, when moving from high to low surface tension (right to left in Figure 7), the threshold forces are reduced (likely a function of less driving-force energy being "wasted" to change the droplet shape for low surface tension liquids). Similarly, saturation forces also decrease as surface tension is reduced, shifting the overall

DOI: 10.1021/acs.langmuir.9b00220
Langmuir 2019, 35, 5342−5352

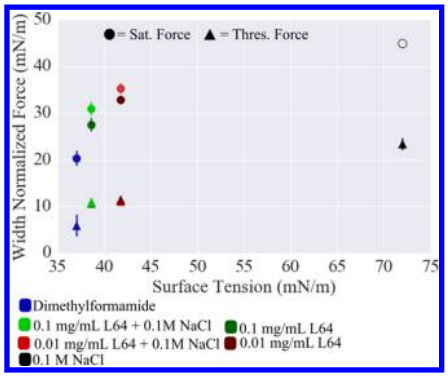

Figure 7. Force windows for optimal digital microfluidic device operation. Width-normalized threshold (filled triangles) and velocity-saturation forces (filled circles) as a function of surface tension for droplets of dimethylformamide (blue) and aqueous droplets containing 0.1 mg/mL L64 (dark green), 0.01 mg/mL L64 (dark red), 0.1 mg/mL L64 (dark green) + 0.1 M NaCl (light green), 0.01 mg/mL L64 + 0.1 M NaCl (light red), and 0.1 M NaCl (black). Error bars indicate ±1 SD for at least $n = 8$ measurements per condition. No saturation force was observed for 0.1 M NaCl (see text for details); the open black circle indicates the maximum force that was tested.

force-window positions for such liquids substantially. In addition, velocity-sensitive dissipation coefficients (k_d, not shown in Figure 7) are observed to increase as surface tension decreases, which reduces the maximum velocities of these fluids.

The data in Figure 7 suggest an interesting conclusion—optimum operating conditions vary dramatically for liquids with different surface tensions, which implies that users should carefully choose diffferent operating conditions (before or during a given experiment) depending on the reagents being used. Thankfully, the analyses described here (including force–velocity plots and force windows) are straightforward to generate by users and experts alike.

CONCLUSIONS

Driving forces that cause droplets to move in digital microfluidics are well understood; resistive forces that oppose movement are not. We have probed these phenomena by characterizing the velocities of droplets manipulated by DMF as a function of applied driving force. Importantly, we observe a velocity saturation effect at high forces, as well as observations of physical phenomena (including satellite-droplet ejection and modulation of device hydrophobicity) that mirror those described in the sessile droplet/electrowetting literature for contact angle saturation. Force–velocity plots for different types of liquids were used to determine the operable force windows (bound by saturation and threshold forces) for different types of liquids, revealing an intriguing relationship between optimum operating conditions and liquid surface tension. Because these methods are simple to use and can be automatically integrated into existing experiments (e.g., as a pre-experiment calibration or as a means of tracking changes in resistive forces over the course of an experiment), they have the potential to provide a wealth of data with minimal effort on the part of users. It is our hope that these methods will make it straightforward for users of DMF to conduct experiments under optimal conditions and perhaps to answer some of the outstanding questions concerning the underlying physical phenomena.

EXPERIMENTAL SECTION

Reagents and Materials. Unless otherwise specified, reagents were purchased from Sigma-Aldrich (Oakville, ON), and deionized (DI) water had an initial resistivity of at least 18 MΩ cm. Pluronic L64 (BASF Corp., Germany) was generously donated by Brenntag Canada (Toronto, ON), and concentrations used here were all well below the CMC of L64, which has been reported as 100 mg/mL.[49] All DMF experiments were carried out using the open-source DropBot hardware (version 2.1, https://github/wheeler-microfluidics/dropbot) and MicroDrop software (version 1.0, https://github/wheeler-microfluidics/microdrop) described previously.[50] DMF device bottom plates featured chromium driving electrodes coated with Parylene C and Teflon AF (and top plates featured a contiguous indium tin oxide electrode coated with Teflon AF), with dimensions designed to match those used in the model (described below), and were fabricated as described previously.[50]

Model of Droplet Dynamics. All analyses were implemented with Python (version 3.5.2) using the numpy (matrix algebra) and pandas (time series) packages. Electrical driving forces were estimated using the electromechanical model for a device geometry that was designed to match the devices used in experiments, with rectangular bottom-plate electrodes ($w = 2.25$ and $L = 5$ mm) coated with a dielectric layer with a thickness d of 5 μm and ϵ_{par} of 3.10. The interplate spacer height was 180 μm, and the model assumed a width-normalized threshold force f_{thres} of 10 mN/m.

Characterization of Droplet Movement. To ensure accurate voltage and capacitance measurements, the DropBot system was calibrated before each set of experiments according to the instructions found on the DropBot wiki (https://github.com/wheeler-microfluidics/dropbot/wiki/ControlBoard). In each experiment, a 2.8 μL droplet was initially positioned on an origin electrode on a DMF bottom plate (adjacent to a destination electrode), and then a top plate was positioned above it (sandwiching the droplet between the two plates).

Prior to droplet movement, the capacitances of an empty electrode (i.e., one covered by filler fluid, in this case, air) and an electrode covered by a droplet were measured and normalized with respect to the length of the electrode, giving the capacitances per unit length, C_{filler} and C_{liquid}, respectively. This calibration data was used to automatically adjust the driving voltage to correspond to the desired force and calculate the droplet position for all measurements in this work. A driving voltage (sine wave at 10 kHz, a frequency found to be within the electrowetting regime[44,45]—such that the electric potential drops across the dielectric layer rather than the droplet—for all of the solutions tested here) was applied to the destination electrode. During this time, capacitance measurements were collected from the destination electrode every 8–15 ms, using an improved version of the circuit described by Fobel et al.[50] (see DropBot version 2.1, https://github/wheeler-microfluidics/dropbot). Droplet positions along the axis of movement x were calculated from the measured capacitance $C_{measured}$ using the following formula.

$$x = \frac{C_{measured} - C_{filler}L}{C_{liquid} - C_{filler}}$$

To generate a force–velocity plot, a droplet was shuttled back and forth between an electrode pair (with each electrode alternately serving as "origin" or "destination") at progressively higher forces, during which the capacitance (and thus position, as above) as a function of time was recorded. Specifically, each actuation step had a duration of 2 s, and the width-normalized driving force in the first step was programmed to be 12 mN/m. The force was then incremented by 1 mN/m per step until the desired stopping force was reached. A 3rd order Savitzky–Golay filter[51] was applied to the position data collected during the step with a window of seven elements starting at the fifth element in the data. To ensure that the velocities measured did not include the period in which the droplet slows down (as it reaches the end of the destination electrode), measurements made when droplet position $x_{droplet} > 0.8L$ were excluded. Instantaneous velocities v_{inst} (i.e., the discrete measurements collected within each

DOI: 10.1021/acs.langmuir.9b00220
Langmuir 2019, 35, 5342–5352

step) were calculated for each position (x_i) and time (t_i) pair using the formula $v_{inst} = (x_i - x_{i-1})/(t_i - t_{i-1})$ and were then smoothed using a 4-point moving average. The terminal velocity for each step was defined as $0.8L$ divided by the final time in the series.

Force−velocity plots were generated by plotting the terminal velocity observed for each step as a function of the applied driving force. This trend is linear at low forces, and when fitted with a linear regression, the threshold force is defined as the x-intercept of the fit. In some cases, driving forces were increased to a level at which the terminal velocity deviated from its initial slope; we called the force at which this occurred the saturation force (F_{sat} or f_{sat} when normalized by electrode width). This point was determined by splitting a given force−velocity plot data set into a series of pairs of subsets (each pair split at a different force step) and performing a linear regression on each subset. The R^2 values of each fit in the series were recorded, and f_{sat} was defined as the step that generated two subset regressions with the highest combination of R^2 values. In some cases, user intervention was required to tweak the determination of f_{sat} (important when particularly nonlinear velocity trends were observed at high driving forces).

Force−velocity plots were generated (and threshold and saturation forces were determined) for a number of different liquids, including DI water with 0.1 M NaCl, DI water with 0.1 M NaCl and 0.1 or 0.01 mg/mL Pluronic L64, DI water with 0.1 or 0.01 mg/mL L64, and pure dimethylformamide (surface tensions for these fluids were taken from the literature[52−54]). In these experiments, a minimum of four droplets of each liquid was evaluated on four different electrode pairs, representing a total of at least eight measurements (one per electrode in each electrode pair) per solution.

Finally, to evaluate the correlation between velocity and capacitance, 2.8 μL droplets of an aqueous solution of 0.1 mg/mL L64 and 0.1 M NaCl were driven from an origin to a destination electrode by applying width-normalized driving forces of 15, 22, or 30 mN/m, during which videos were captured with a Nexus 5X phone camera through the 10× eye piece of a dissection microscope equipped with a 4× zoom using a ring illumination light source. The relevant position and velocity data generated from capacitance measurements were then compared to positions and velocities determined from corresponding steps in the videos. All other videos and images of droplet movement and ejection were collected identically but using a 20× eye piece. Three such movies (Videos M1−M3) are included in the Supporting Information.

Contact Angle Measurements. To evaluate the effects of velocity saturation on device surfaces, a 2.8 μL droplet of an aqueous solution with 0.1 M NaCl, 0.01 mg/mL L64 + 0.1 M NaCl, or 0.1 mg/mL L64 + 0.1 M NaCl was driven back and forth between a single electrode pair at a width-normalized driving force of 25, 30, or 35 mN/m for 20 min. After actuation, the top plate was removed and the bottom plate surfaces were rinsed gently with DI water. After air drying, two 3 μL droplets of DI water were placed separately on each electrode on the bottom plate and the contact angles were determined using a Krüss DSA 100 employing the tangent method. Contact angle measurements were collected for three different droplets on each electrode in the pair (representing a total of six contact angle measurements). This process was repeated twice more (each time with fresh DI water droplets on fresh electrodes), representing a total of 18 measurements for each force/solution pairing.

■ ASSOCIATED CONTENT

Supporting Information

The Supporting Information is available free of charge on the ACS Publications website at DOI: 10.1021/acs.langmuir.9b00220.

Supplementary videos M1, M2, and M3 illustrating movement steps for different liquids collected during the generation of force-velocity curves, with width-normalized driving forces indicated. M1 depicts an aqueous droplet containing 0.1 mg/mL L64 in real time. A white arrow highlights droplet ejection beginning at around 30 mN/m. M2 depicts a droplet of dimethylformamide, with droplet ejection beginning at around 20 mN/m. Most of the frames in M2 are presented in real time; the 42 mN/m step is presented in slow motion to permit more detailed observation of droplet ejection. M3 depicts a droplet containing 0.1 M NaCl + 0.1 mg/mL L64 in real time. (ZIP)

Analysis of the experimental system described here in terms of the nondimensional Weber, Reynolds, and capillary numbers; discussion of the time constants associated with the electrical circuit and droplet acceleration; detailed analysis of the relationship between capacitance and optical measurements of droplet position; raw data for all replicate force−velocity curves (PDF)

■ AUTHOR INFORMATION

Corresponding Author

*E-mail: aaron.wheeler@utoronto.ca.

ORCID

Aaron R. Wheeler: 0000-0001-5230-7475

Author Contributions

‖These authors contributed equally.

Notes

The authors declare the following competing financial interest(s): R.F. and A.R.W. are co-founders of startup company, Sci-Bots Inc., that sells a commercial version of the DropBot system that is described herein. But the actual DropBot instruments used for this work were home-made by members of the lab, and can be reproduced as "open source hardware" by any interested party. For details, see http://microfluidics.utoronto.ca/dropbot/.

■ ACKNOWLEDGMENTS

We thank Prof. Frieder Mugele (University of Twente) for fruitful discussions and advice. We thank the Natural Sciences and Engineering Research Council of Canada (NSERC) for funding and Prof. Eugenia Kumacheva (University of Toronto) for access to her contact angle goniometer. A.R.W. thanks the Canada Research Chair (CRC) Program for a CRC.

■ REFERENCES

(1) Pollack, M. G.; Fair, R. B.; Shenderov, A. D. Electrowetting-based actuation of liquid droplets for microfluidic applications. *Appl. Phys. Lett.* **2000**, *77*, 1725−1726.

(2) Cho, S. K.; Moon, H.; Kim, C.-J. Creating, transporting, cutting, and merging liquid droplets by electrowetting-based actuation for digital microfluidic circuits. *J. Microelectromech. Syst.* **2003**, *12*, 70−80.

(3) Wheeler, A. R. Putting Electrowetting to Work. *Science* **2008**, 539−540.

(4) Atabakhsh, S.; Ashtiani, S. J. Thermal actuation and confinement of water droplets on paper-based digital microfluidics devices. *Microfluid. Nanofluid.* **2018**, *22*, 43.

(5) Jiao, Z.; Huang, X.; Nguyen, N.-T.; Abgrall, P. Thermocapillary actuation of droplet in a planar microchannel. *Microfluid. Nanofluid.* **2008**, *5*, 205−214.

(6) Shin, D. J.; Wang, T.-H. Magnetic droplet manipulation platforms for nucleic acid detection at the point of care. *Ann. Biomed. Eng.* **2014**, *42*, 2289−2302.

(7) Zhang, Y.; Wang, T.-H. Full-Range Magnetic Manipulation of Droplets via Surface Energy Traps Enables Complex Bioassays. *Adv. Mater.* **2013**, *25*, 2903−2908.

DOI: 10.1021/acs.langmuir.9b00220
Langmuir 2019, 35, 5342−5352

(8) Chen, C.; Zhang, S. P.; Mao, Z.; Nama, N.; Gu, Y.; Huang, P.-H.; Jing, Y.; Guo, X.; Costanzo, F.; Huang, T. J. Three-dimensional numerical simulation and experimental investigation of boundary-driven streaming in surface acoustic wave microfluidics. *Lab Chip* **2018**, *18*, 3645−3654.
(9) Holmes, H. R.; Böhringer, K. F. Transport velocity of droplets on ratchet conveyors. *Adv. Colloid Interface Sci.* **2018**, *255*, 18−25.
(10) Eydelnant, I. A.; Li, B. B.; Wheeler, A. R. Microgels on-demand. *Nat. Commun.* **2014**, 3355.
(11) Ng, A. H. C.; Chamberlain, M. D.; Situ, H.; Lee, V.; Wheeler, A. R. Digital microfluidic immunocytochemistry in single cells. *Nat. Commun.* **2015**, 7513.
(12) Chiang, M.-Y.; Hsu, Y.-W.; Hsieh, H.-Y.; Chen, S.-Y.; Fan, S.-K. Constructing 3D heterogeneous hydrogels from electrically manipulated prepolymer droplets and crosslinked microgels. *Sci. Adv.* **2016**, *2*, No. e1600964.
(13) Jebrail, M. J.; Ng, A. H. C.; Rai, V.; Hili, R.; Yudin, A. K.; Wheeler, A. R. Synchronized Synthesis of Peptide-Based Macrocycles by Digital Microfluidics. *Angew. Chem., Int. Ed.* **2010**, *49*, 8625−8629.
(14) Keng, P. Y.; Chen, S.; Ding, H.; Sadeghi, S.; Shah, G. J.; Dooraghi, A.; Phelps, M. E.; Satyamurthy, N.; Chatziioannou, A. F.; Kim, C.-J. C.; van Dam, R. M. Micro-chemical synthesis of molecular probes on an electronic microfluidic device. *Proc. Natl. Acad. Sci.* **2012**, *109*, 690−695.
(15) Sista, R. S.; Wang, T.; Wu, N.; Graham, C.; Eckhardt, A.; Winger, T.; Srinivasan, V.; Bali, D.; Millington, D. S.; Pamula, V. K. Multiplex Newborn Screening for Pompe, Fabry, Hunter, Gaucher, and Hurler Diseases Using a Digital Microfluidic Platform. *Clin. Chim. Acta* **2013**, *424*, 12−18.
(16) Ng, A. H. C.; Lee, M.; Choi, K.; Fischer, A. T.; Robinson, J. M.; Wheeler, A. R. Digital Microfluidic Platform for the Detection of Rubella Infection and Immunity: A Proof of Concept. *Clin. Chem.* **2015**, *61*, 420−429.
(17) Ng, A. H. C.; et al. A digital microfluidic system for serological immunoassays in remote settings. *Sci. Transl. Med.* **2018**, No. eaar6076.
(18) Jones, T. B. On the Relationship of Dielectrophoresis and Electrowetting. *Langmuir* **2002**, 4437−4443.
(19) Kang, K. H. How Electrostatic Fields Change Contact Angle in Electrowetting. *Langmuir* **2002**, 10318−10322.
(20) Jones, T. B.; Wang, K.-L.; Yao, D. J. Frequency-Dependent Electromechanics of Aqueous Liquids: Electrowetting and Dielectrophoresis. *Langmuir* **2004**, 2813−2818.
(21) Chatterjee, D.; Hetayothin, B.; Wheeler, A. R.; King, D. J.; Garrell, R. L. Droplet-based microfluidics with nonaqueous solvents and solutions. *Lab Chip* **2006**, 199−206.
(22) Chatterjee, D.; Shepherd, H.; Garrell, R. L. Electromechanical model for actuating liquids in a two-plate droplet microfluidic device. *Lab Chip* **2009**, 1219−1229.
(23) Ren, H.; Fair, R. B.; Pollack, M. G.; Shaughnessy, E. J. Dynamics of electro-wetting droplet transport. *Sens. Actuators, B* **2002**, 201−206.
(24) Blake, T. D.; Haynes, J. M. Kinetics of Displacement. *J. Colloid Interface Sci.* **1969**, *30*, 421−423.
(25) Wang, K. L.; Jones, T. B. Electrowetting Dynamics of Microfluidic Actuation. *Langmuir* **2005**, 4211−4217.
(26) 't Mannetje, D. J. C. M.; Murade, C. U.; van den Ende, D.; Mugele, F. Electrically assisted drop sliding on inclined planes. *Appl. Phys. Lett.* **2011**, *98*, No. 014102.
(27) Lu, H.-W.; Bottausci, F.; Fowler, J. D.; Bertozzi, A. L.; Meinhart, C.; Kim, C.-J. A Study of EWOD-Driven Droplets by PIV Investigation. *Lab Chip* **2008**, *8*, 456−461.
(28) Kinoshita, H.; Kaneda, S.; Fujii, T.; Oshima, M. Three-dimensional measurement and visualization of internal flow of a moving droplet using confocal micro-PIV. *Lab Chip* **2007**, 338−346.
(29) Song, J. H.; Evans, R.; Lin, Y.-Y.; Hsu, B.-N.; Fair, R. B. A scaling model for electrowetting-on-dielectric microfluidic actuators. *Microfluid. Nanofluid.* **2009**, 75−89.
(30) Jain, V.; Hole, A.; Deshmukh, R.; Patrikar, R. Dynamic capacitive sensing of droplet parameters in a low-cost open EWOD system. *Sens. Actuators, A* **2017**, *263*, 224−233.
(31) Bavière, R.; Boutet, J.; Fouillet, Y. Dynamics of droplet transport induced by electrowetting actuation. *Microfluid. Nanofluid.* **2008**, *4*, 287−294.
(32) Mugele, F.; Herminghaus, S. Electrostatic stabilization of fluid microstructures. *Appl. Phys. Lett.* **2002**, *81*, 2303−2305.
(33) Vallet, M.; Vallade, M.; Berge, B. Limiting phenomena for the spreading of water on polymer films by electrowetting. *Eur. Phys. J. B* **1999**, *11*, 583−591.
(34) Verheijen, H. J. J.; Prins, M. W. J. Reversible Electrowetting and Trapping of Charge: Model and Experiments. *Langmuir* **1999**, *15*, 6616−6620.
(35) Papathanasiou, A. G.; Papaioannou, A. T.; Boudouvis, A. G. Illuminating the connection between contact angle saturation and dielectric breakdown in electrowetting through leakage current measurements. *J. Appl. Phys.* **2008**, *103*, No. 034901.
(36) Drygiannakis, A. I.; Papathanasiou, A. G.; Boudouvis, A. G. On the Connection between Dielectric Breakdown Strength, Trapping of Charge, and Contact Angle Saturation in Electrowetting. *Langmuir* **2009**, *25*, 147−152.
(37) Raj, B.; Dhindsa, M.; Smith, N. R.; Laughlin, R.; Heikenfeld, J. Ion and liquid Dependent dielectric failure in electrowetting systems. *Langmuir* **2009**, *25*, 12387−12392.
(38) Chevalliot, S.; Malet, G.; Keppner, H.; Berge, B. Insulating material requirements for low-power-consumption electrowetting-based liquid lenses. *Langmuir* **2016**, *32*, 13585−13592.
(39) Narasimhan, V.; Park, S.-Y. An ion gel as a low-cost, spin-coatable, high-capacitance dielectric for electrowetting-on-dielectric (EWOD). *Langmuir* **2015**, *31*, 8512−8518.
(40) Baird, E.; Mohseni, K. Digitized heat transfer: a new paradigm for thermal Management of compact micro systems. *IEEE Trans. Compon. Packag. Technol.* **2008**, *31*, 143−151.
(41) Schertzer, M. J.; Gubarenko, S. I.; Ben-Mrad, R.; Sullivan, P. E. An empirically validated analytical model of droplet dynamics in electrowetting on dielectric devices. *Langmuir* **2010**, *26*, 19230−19238.
(42) Nelson, W. C.; Kim, C.-J. Droplet actuation by electrowetting-on-dielectric (EWOD): A review. *J. Adhes. Sci. Technol.* **2012**, *26*, 1747−1771.
(43) Blake, T. D. The physics of moving wetting lines. *J. Colloid Interface Sci.* **2006**, *299*, 1−13.
(44) Choi, K.; Ng, A. H. C.; Fobel, R.; Wheeler, A. R. Digital microfluidics. *Annual review of Analytical Chemistry* **2012**, *5*, 413−440.
(45) Fan, S.-K.; Hsu, Y.-W.; Chen, C.-H. Encapsulated droplets with metered and removable oil shells by electrowetting and dielectrophoresis. *Lab Chip* **2011**, *11*, 2500−2508.
(46) Au, S. H.; Kumar, P.; Wheeler, A. R. A new angle on pluronic additives: advancing droplets and understanding in digital microfluidics. *Langmuir* **2011**, *27*, 8586−8594.
(47) Luk, V. N.; Fiddes, L. K.; Luk, V. M.; Kumacheva, E.; Wheeler, A. R. Digital microfluidic hydrogel microreactors for proteomics. *Proteomics* **2012**, *12*, 1310−1318.
(48) Sarvothaman, M. K.; Kim, K. S.; Seale, B.; Brodersen, P. M.; Walker, G. C.; Wheeler, A. R. Dynamic Fluoroalkyl Polyethylene Glycol Co-Polymers: A New Strategy for Reducing Protein Adhesion in Lab-on-a-Chip Devices. *Adv. Funct. Mater.* **2015**, *25*, 506−515.
(49) Alexandridis, P.; Hatton, T. A. Poly(ethylene oxide)—poly(propylene oxide)—poly(ethylene oxide) block copolymer surfactants in aqueous solutions and at interfaces: thermodynamics, structure, dynamics, and modeling. *Colloids Surf., A* **1995**, *96*, 1−46.
(50) Fobel, R.; Fobel, C.; Wheeler, A. R. DropBot: An open-source digital microfluidic control system with precise control of electrostatic driving force and instantaneous drop velocity measurement. *Appl. Phys. Lett.* **2013**, *102*, 193513.
(51) Savitzky, A.; Golay, M. J. E. Smoothing and Differentiation of Data by Simplified Least Squares Procedures. *Anal. Chem.* **1964**, *36*, 1627−1639.

DOI: 10.1021/acs.langmuir.9b00220
Langmuir 2019, 35, 5342−5352

(52) Haynes, W. M. *CRC Handbook of chemistry and Physics*; CRC Press: 2015.
(53) Prasad, K. N.; Luong, T. T.; Paris, A. T. F.; Vaution, C.; Seiller, M.; Puisieux, F. Surface activity and association of ABA polyoxyethylene-polyoxypropylene block copolymers in aqueous solution. *J. Colloid Interface Sci.* **1979**, *69*, 225−232.
(54) Weissenborn, P. K.; Pugh, R. J. Surface tension of aqueous solutions of electrolytes: relationship with ion hydration, oxygen solubility, and bubble coalescence. *J. Colloid Interface Sci.* **1996**, *184*, 550−563.

DOI: 10.1021/acs.langmuir.9b00220
Langmuir 2019, 35, 5342−5352